Sensors and Materials, Vol. 37, No. 10 (2025) 4335–4346
MYU Tokyo

S & M 4185

Design and Calibration of a Three-axis Intraoperative Force Sensor for Reverse Total Shoulder Arthroplasty

Yusuke Hirai,* Yuta Onishi, and Masaru Higa

Department of Mechanical Engineering, University of Hyogo, 2167 Shosha, Himeji 671-2280, Japan

(Received June 2, 2025; accepted July 17, 2025)

Keywords: biomechanics, reverse total shoulder arthroplasty, joint contact force, instrumented prosthesis

Inadequate soft tissue tension around the shoulder joint is the known cause of postoperative complications following reverse total shoulder arthroplasty (RTSA). However, this tension is not currently quantified intraoperatively. Understanding soft tissue tension can help surgeons choose the appropriate implant size and alignment, potentially reducing the risk of complications. To address this, we developed a force sensor that measures joint contact force in the shoulder to estimate soft tissue tension. The force sensor includes strain gauges and a printed circuit board for analog-to-digital conversion. It is waterproof and can be sterilized, making it suitable for use during surgery. In this study, we present the force sensor's design, results from the finite element analysis of output strain values of a sensing element, and calibration results. The results of the strain analysis showed a strong correlation between the output strain and the applied force, with correlation coefficients above 0.999 across all three axes (X, Y, and Z). As a result of the calibration, the correlation coefficients were 0.8284 on the X-axis, 0.8078 on the Y-axis, and 0.9413 on the Z-axis. The maximum errors were 8.5 N on the X-axis, −13 N on the Y-axis, and −6.1 N on the Z-axis. Although the errors are large, this force sensor is useful for quantifying soft tension tissue during RTSA.

1. Introduction

Reverse total shoulder arthroplasty (RTSA) is a treatment used for a variety of shoulder conditions including rotator cuff tear, fracture, rheumatoid arthritis, and failed total shoulder arthroplasty.[1–4] RTSA was approved for clinical use in the United States in 2004 and in Japan in 2014, and the number of surgeries has increased.[5] Although RTSA has become widespread, many complications have been reported. In a study of 4158 patients with RTSA, the postoperative complication rate was 8.9%, and the top three complications were pain due to acromion/scapula fractures after 11 months, instability after 16 months, and pain after 17 months.[6] Another study showed that 5% of patients presented with instability after two years and 7.5% with dislocation after three years.[7] There are several causes of complications, one of which is inadequate soft tissue tension around the shoulder joint.[8] Undertensioned RTSA can lead to dislocation,

*Corresponding author: e-mail: ev23m501@guh.u-hyogo.ac.jp
https://doi.org/10.18494/SAM5766

ISSN 0914-4935
https://myukk.org/

whereas overtensioned RTSA can also lead to complications such as acromial fracture or brachial plexus injury.[9]

To achieve proper soft tissue tension during surgery, which is important for good clinical outcomes, surgeons choose various implant designs, sizes, placements, and orientations. Soft tissue tension can be quantified by measuring joint contact force as counteraction force. In the past, we measured the joint contact force of RTSA intraoperatively using a force-sensor-instrumented prosthesis,[10] but the force sensor was connected by screws, making the measurement cumbersome. The force sensors reported in other research groups' studies were fixed directly to the humerus and could not be easily attached or removed.[11–13] There were also studies on the intraoperative measurement of shoulder joint contact force, but no detailed structure and accuracy were reported, and they are currently no longer available.[14] The required force range and accuracy of the force sensor in RTSA are currently not well established. A previous study conducted in the United States reported force ranging from 100 to 200 N.[9,15–17] However, since our force sensor is primarily intended for use in Japan, we expect that the measured forces will be lower owing to the differences observed in patients. Regarding accuracy, the maximum error of the force sensors used in the studies was approximately 30 N,[16,17] indicating that improvement is necessary.

The purpose of this study was to quantify soft tissue tension around the shoulder joint during RTSA. Therefore, we have developed a three-axis force-sensor-instrumented prosthesis that has built-in strain gauges and can measure shoulder joint contact force intraoperatively. This force sensor can be used in trials and can be easily attached and removed from the shoulder joint implant. In this report, we describe the design of the force sensor and the accuracy of its measurements through calibrations.

2. Materials and Methods

2.1 Materials

The force-sensor-instrumented prosthesis was designed to be used with an existing RTSA system (EQUINOXE, Exactech Inc, USA), just as a standard trial implant. We used a trial humeral liner, which is easily attached and removed [Fig. 1(a)]. The force sensor comprises an upper part (made of SUS303), a bottom part (made of SUS303), a sensing element (made of SUS303), six uniaxial foil strain gauges (EFLK-02-11-002LE, Tokyo Sokki Kenkyujo Co., Ltd., Japan), a printed circuit board (PCB), and a bundle of cables (Fig. 1). The bottom part was fixed to the standard humeral tray, and the upper part moved when a contact force from the glenosphere was applied. These parts were connected by screws via the sensing element, which is designed to be more deformable than the upper and bottom parts. A silicone gasket was sandwiched between the upper and bottom parts for sealing and as a stopper against overload. The strains of the sensing element were measured using six strain gauges. Other peripheral circuits including bridges, amplifiers, and analog-to-digital (A/D) converters (ADCs) were mounted on the PCB. Since A/D conversions are completed inside the force sensor, digital signals are transmitted through cables to a microcomputer (Arduino Mega 2560), so that noise infections can be minimized.

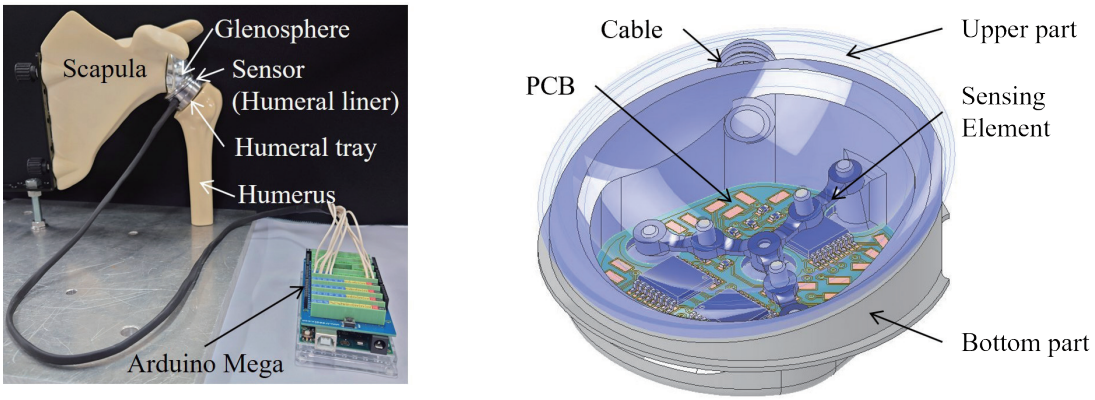

(a) (b)

Fig. 1. (Color online) (a) Whole measurement unit. The force sensor is attached to the RTSA and the outside part (Arduino mega 2560) is connected by cables. (b) 3-D CAD models of the force sensor unit. The upper part is transparent.

2.2 Sensing element design and calibration method

Because the shoulder joint is a ball-and-socket joint, the joint contact force is three-dimensional. We developed the sensing element that consists of three double-ended beams and has three force-measuring elements [Fig. 2(a)]. Each beam was designed to have two thin parts so that deformations occur there, and the strain gauges were attached to those areas. Figures 2(b) and 2(c) show the deformation patterns of the sensing element when external forces are applied. Two strain gauges on a single beam are considered as one unit, and the force direction can be estimated on the basis of the combination of compressive or tensile strain patterns, while the magnitude of the force can be estimated on the basis of the magnitude of the strains.

We verified whether the sensing element structure can obtain sufficient strain to distinguish between three axial forces using the finite element method (FEM). The purpose of FEM is to determine whether Eqs. (4)–(6) are acceptable for calculating three strains: ε_x, ε_y, and ε_z. Figure 3(a) shows the analyzed geometry, the boundary conditions, and the definitions of axes and angles. The four points of the bottom surfaces of the sensing element, which are described in filled triangles, were fixed, and the surfaces of the center of the double-ended beam were assumed to be connected to the upper part. The loading conditions were 25 and 50 N in 33 directions, with (θ) at 12.5 degree intervals from 0 to 50 degrees and (φ) at 45 degree intervals from 0 to 360 degrees. On the surface of the upper part, the forces were applied normally to that surface from the 33 directions. Since the shoulder joint has a spherical shape, we initially intended to apply forces in the *X*-, *Y*-, and *Z*-axis directions from the center of the humeral head. However, owing to the shallow, cup-like shape of the glenosphere, it was not possible to apply a uniaxial force in the *X*- and *Y*-axis directions. Therefore, forces were applied at given polar angle (φ) and azimuthal angle (θ) values. The measured strains are shown in Fig. 3(b). The *X*-axis was set to 0 degrees, and six points were set at the center of every fixed point on the three beams. The output strain values were strains parallel to the X_{30} axis for ε_1 and ε_2, the X_{150} axis for ε_3 and ε_4, and the X_{270} axis for ε_5 and ε_6. Since we use uniaxial strain gauges, only one-dimensional strains parallel to the strain gauges were analyzed.

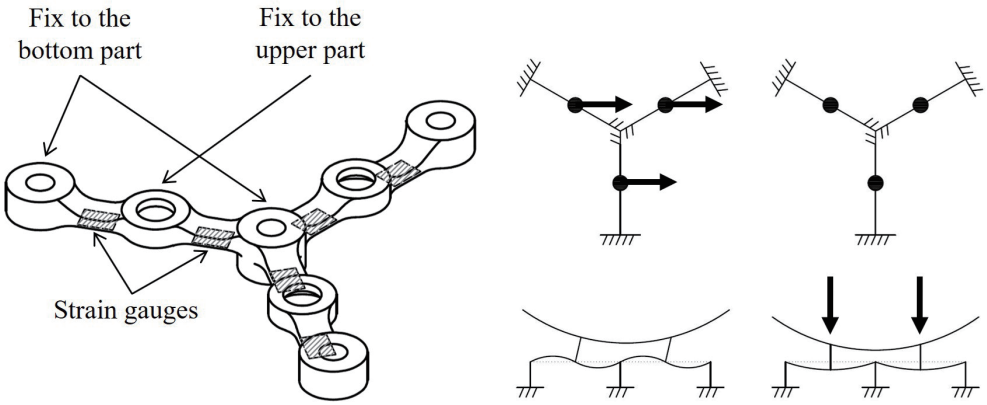

Fig. 2. (a) Whole image of sensing element with strain gauges, which has three beams. The center and three ends of the sensing element are fixed to the bottom part, and the middle holes of the beams are fixed to the upper part. Six strain gauges were attached to one side of the beam indicated by hatchings. The deformation patterns of the sensing element were described when forces were applied in the (b) horizontal and (c) vertical directions. The upper figures show the top view of the sensing element, and the bottom figures show the side view with deformation patterns. Three black circles indicate the center of the double-ended beam, and the arrows indicate the direction of the forces. Diagonal lines indicate the ends of the beams fixed to the bottom part. When a force acts horizontally, the beams are strained in compression and tension, whereas when a force acts vertically, all the strains are in tension.

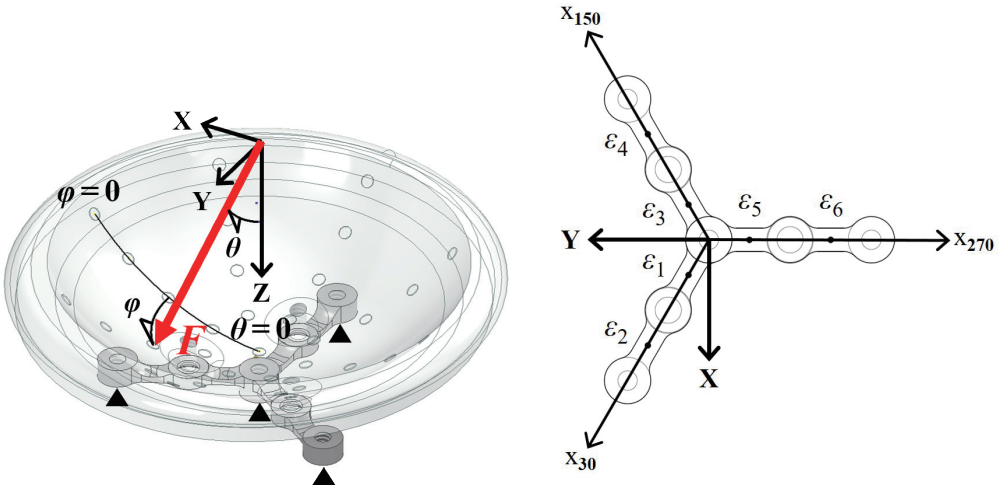

Fig. 3. (Color online) (a) 3-D CAD model used for the analysis and definitions of the axes and angles. The origin of the axes was set at the center of the glenosphere. The polar angle (θ) is defined as the angle between the applied force direction and the Z-axis. The azimuthal angle (φ) is defined as the rotation angle around the Z-axis. (b) Bottom view of sensing element. The black dots indicate the location where the strain was measured.

The applied force F is expressed by Eqs. (1)–(3) using the output strain ε and coefficient C. Cx, Cy, and Cz show positive constant values. The subscripts x, y, and z indicate the X-axis, Y-axis, and Z-axis components, respectively. The output strains ε_x, ε_y, and ε_z are expressed by Eqs. (4)–(6) using the output strain ε_i values (i = 1–6). Tensile strains are positive, whereas

compressive strains are negative. When the force was applied from the positive direction of the *X*-axis, ε_1 and ε_4 would be in compression and ε_2 and ε_3 would be in tension, and the bending direction could be determined by these four output strains (Eq. 5). In the case of the *Y*-axis, the difference in output strain between ε_5 and ε_6 would determine ε_y (Eq. 5). In the *Z*-axis, the sum of all output strains would determine ε_z (Eq. 6). On the *X*-axis, ε_5 and ε_6 have no effect on ε_x. Regarding the *Y*-axis, although the output strain ε_i values (i = 1–4) were also assumed to have an effect on ε_y, they were ignored in calculating ε_y, because it was expected that the axial strains due to bending deformation are larger than those due to tensile or compressive deformation.

$$Fx = Cx\varepsilon_x \tag{1}$$

$$Fy = Cy\varepsilon_y \tag{2}$$

$$Fz = Cz\varepsilon_z \tag{3}$$

$$\varepsilon_x = \left(\varepsilon_2 - \varepsilon_1\right) - \left(\varepsilon_4 - \varepsilon_3\right) \tag{4}$$

$$\varepsilon_y = -\left(\varepsilon_6 - \varepsilon_5\right) \tag{5}$$

$$\varepsilon_z = \left(\varepsilon_1 + \varepsilon_2\right) + \left(\varepsilon_3 + \varepsilon_4\right) + \left(\varepsilon_5 + \varepsilon_6\right) \tag{6}$$

The results of FEM are shown in Fig. 4. The vertical axes show the output strains analyzed by FEM using Eqs. (1)–(6), and the horizontal axes show the applied forces *Fx*, *Fy*, and *Fz*. The applied force *F* was decomposed into *Fx*, *Fy*, and *Fz* components on the basis of the orthogonal coordinate system shown in Fig. 3. Since the loading conditions were defined in polar coordinates, the results should ideally be organized on the basis of the polar coordinates and the angles φ and θ. However, to evaluate Eqs. (1)–(6) as assumed in this study, the relationships between the output strain and *Fx*, *Fy*, and *Fz* were organized. The approximation curves were calculated by the least squares method. When the correlation coefficients between the applied force and the output strain were calculated, the linear correlation coefficients were above 0.999 in all directions. As shown in these three charts, the applied force and ε have linear correlations expressed in Eqs. (1)–(3). The coefficient *C* values were *Cx* = 0.023, *Cy* = 0.040, and *Cz* = 0.025. At the applied force of 50 N, the changes in ε_x, ε_y, and ε_z were approximately ± 2000 $\mu\varepsilon$, ± 1000 $\mu\varepsilon$, and + 2000 $\mu\varepsilon$, respectively. When resultant forces were applied, *Fx*, *Fy*, and *Fz* were accurately calculated from the output strains ε_x, ε_y, and ε_z. For example, when ε_x was 1000 $\mu\varepsilon$, ε_y was 500 $\mu\varepsilon$, and ε_z was 1000 $\mu\varepsilon$, the applied force *F* values were calculated from Eqs. (1)–(3) as *Fx* = 23 N, *Fy* = 20 N, and *Fz* = 25 N.

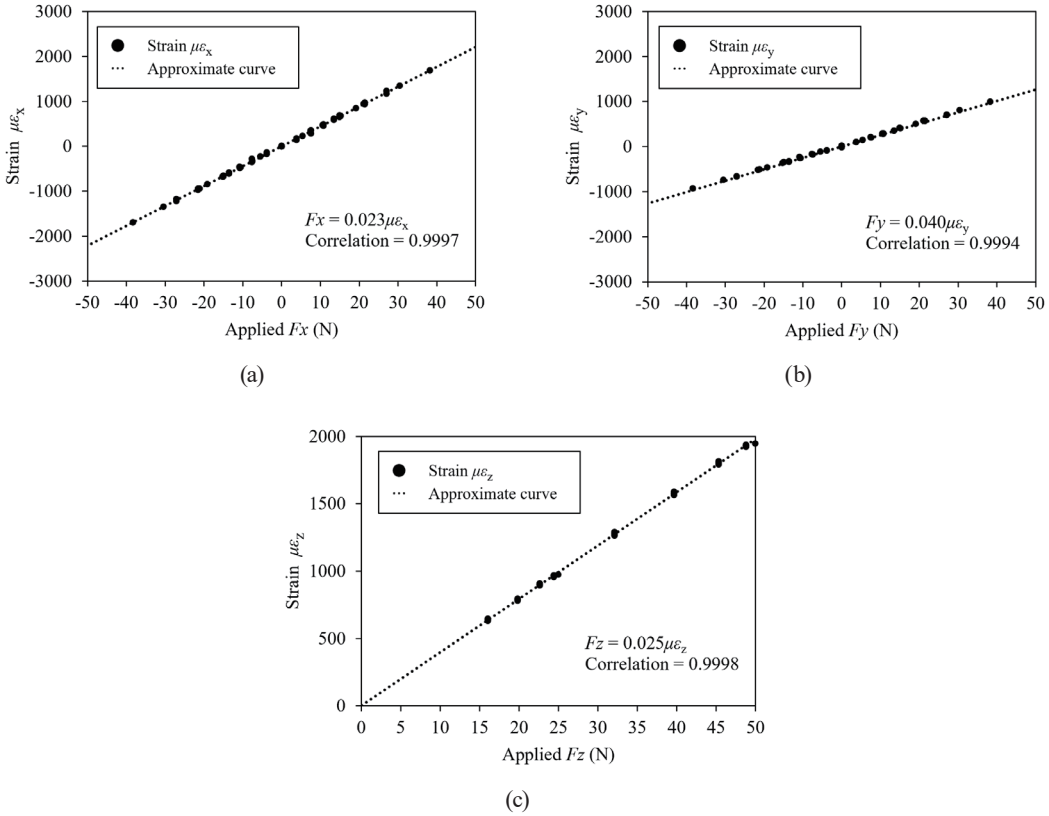

Fig. 4. Output strain plotted against applied force. These figures show (a) ε_x vs Fx, (b) ε_y vs Fy, and (c) ε_z vs Fz. The vertical axes of each diagram represent the output strains. The dotted line is an approximation curve obtained by the least squares method to fit the output strains and to pass through the origin (0, 0). The correlation coefficients between the output strains and the applied forces are shown.

2.3 PCB design

Figure 5(a) shows the circuit diagram of the PCB. Six Wheatstone bridges were used to measure the resistance of the strain gauges. Because 120 Ω strain gauges were used, the Wheatstone bridge circuit also used 120 Ω chip resistors with an accuracy of ± 0.1% (ERA-2VEB1200X, Panasonic Industry Co., Ltd., Japan), and the excitation voltage was set at 3.3 V. The output voltage of the Wheatstone bridge circuit was measured with a differential input using a 24-bit ADC (ADS122U04, Texas Instruments Inc, USA). The 24-bit ADC has four analog input channels and supports two differential input channels, and has a programmable gain amplifier (PGA) function and amplifies the output voltage up to 128 times. In the case of PGA 128 A/D conversion with the ADC internal voltage as a reference, the full-scale range (FSR) of the conversion voltage is ± 16 mV according to the ADC datasheet. The relationship between the output strain ε and the output voltage E_0 in the Wheatstone bridge circuit is expressed as

$$E0 = \frac{1}{4} K \varepsilon Ve \text{ or } \varepsilon = \frac{4E0}{KVe}, \tag{7}$$

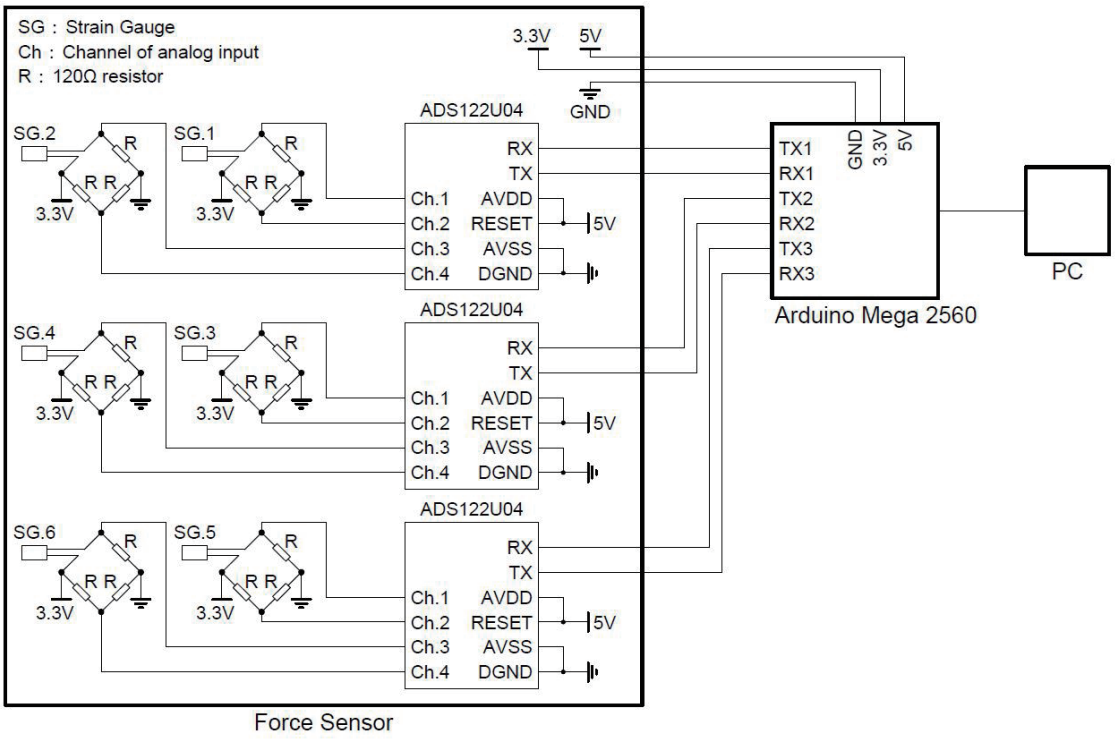

(a)

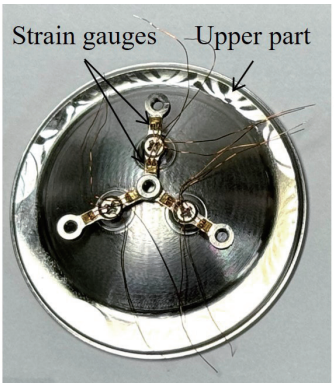

(b)

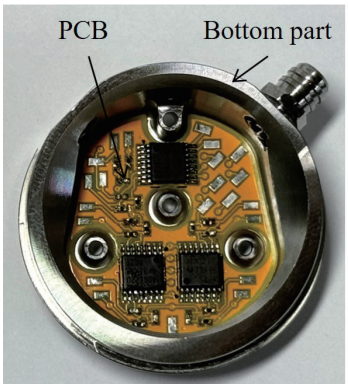

(c)

Fig. 5. (Color online) (a) Circuit diagram of PCB. The PCB was composed of six Wheatstone bridge circuits and three ADCs that transmitted measurement data to the Arduino Mega 2560 via serial communication. (b) Photograph of upper part and sensing element with strain gauges. (c) Photograph of PCB set at the bottom. The PCB has three ADS122U04 and chip resistors for the bridge circuit soldered to it. The strain gauge wires and communication cables are yet to be soldered to the vacant pads.

where K is the gauge factor ($K = 2.2$) and V_e the excitation voltage ($V_e = 3.3$ V).[18] According to the results of FEM analysis, the output strain of the force sensor is approximately ± 2500 $\mu\varepsilon$; therefore, the output voltage E_0 range is ± 4.6 mV. If the force is below 50 N, the output voltage never exceeds the limit. The voltage resolution is 1.9 μV, since the ADC is 24 bit and the FSR is ± 16 mV. By substituting 1.9×10^{-6} V for E_0, 2.2 for K, and 3.3 V for V_e into Eq. (7) and

converting the output strain, the output strain is calculated to be approximately 1 $\mu\varepsilon$. Therefore, the strain resolution of this PCB is considered to be approximately 1 $\mu\varepsilon$.

The analog circuits such as the strain gauges and Wheatstone bridge circuits were designed to be as small as possible to reduce noise. Therefore, the PCB containing six strain gauges, six Wheatstone bridge circuits, and three ADCs were mounted inside the force sensor [Figs. 5(b) and 5(c)]. Owing to the limited rooms inside the force sensor, only the necessary components were mounted on the PCB. The three ADCs were connected to the Arduino Mega 2560, which continuously obtains measurement values from the three ADCs with a sampling rate of 15 Hz.

2.4 Experiments

Figure 6 shows the experimental setup for calibrating the force sensor. The force sensor was mounted on the humeral tray, which was screwed to the jig, and the jig was fixed on an angle vise. The jig was cut into an octagonal cross section, and the azimuthal angle (φ) was changed by selecting different surfaces to clamp in the angle vise. The polar angle (θ) was set by adjusting the angle of the angle vise. The azimuthal angle (φ) and polar angle (θ) were the same as defined in the previous FEM (Fig. 3). The angle vise was mounted on two-axis low-friction linear slide rails to eliminate horizontal constraint. Known F values were applied by a testing machine through a 38-mm-diameter half sphere imitating the glenosphere. The known forces were monitored using a load cell attached between the testing machine and the glenosphere. The loading conditions were 10, 20, and 30 N in nine directions, with θ at 0, 10, and 20 degrees, and φ at 0, 90, 180, and 270 degrees. The output strain ε_i values (i = 1–6) were determined by averaging the measurements obtained from 50 samples under a constant applied force. Cx, Cy, and Cz were calculated using Eqs. (1)–(3) and ε_x, ε_y, and ε_z were calculated using Eqs. (4)–(6), respectively.

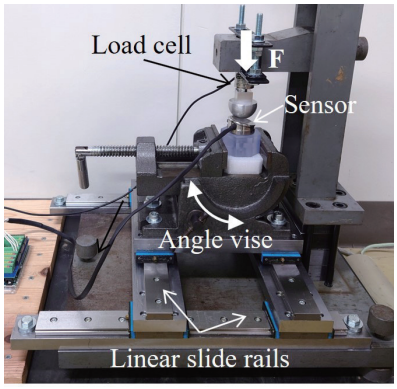

Fig. 6. (Color online) Experimental setup used to calibrate the force sensor. The force sensor was mounted on a custom calibration jig clamped by an angle vise. The entire setup was placed on top of linear two-axis slide rails. Uniaxial load was applied to the force sensor via a glenosphere-shaped sphere, and the load value was monitored using a load cell.

3. Results

The experimental results are shown in Fig. 7. The vertical axes show the output strain values and the horizontal axes show the applied forces *Fx*, *Fy*, and *Fz*. The applied force *F* was decomposed into *Fx*, *Fy*, and *Fz* components on the basis of the orthogonal coordinate system shown in Fig. 3. Although applied forces were described in the polar angle (φ), azimuthal angle (θ), and absolute values of 10, 20, and 30 N, results are expressed in *Fx*, *Fy*, and *Fz* components. The approximation curves were calculated by the least squares method. The linear correlation coefficients were 0.8284 for *Fx*, 0.8078 for *Fy*, and 0.9413 for *Fz*. The coefficient *C* values were $Cx = 0.107$, $Cy = 0.175$, and $Cz = 0.087$. The change in ε_x was from −61 $\mu\varepsilon$ to 131 $\mu\varepsilon$, ε_y was from −95 $\mu\varepsilon$ to 8 $\mu\varepsilon$, and ε_z was from 49 $\mu\varepsilon$ to 433 $\mu\varepsilon$. The largest differences between the approximate curve and the output strain values are as follows: 79 $\mu\varepsilon$ on the *X*-axis (applied $Fx = -10$ N), −72 $\mu\varepsilon$ on the *Y*-axis (applied $Fy = 0$ N), and −82 $\mu\varepsilon$ on the *Z*-axis (applied $Fz = 18$ N). In terms of the difference in force, the differences were 8.5 N on the *X*-axis, −13 N on the *Y*-axis, and −6.1 N on the *Z*-axis.

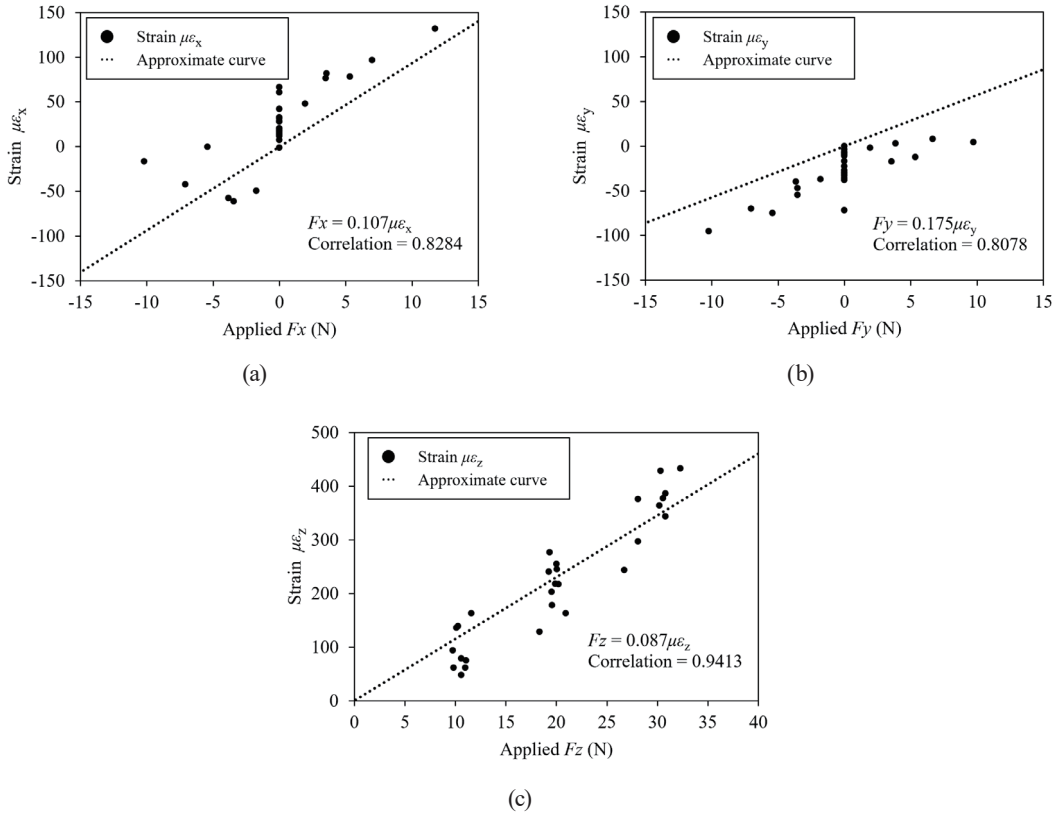

Fig. 7. Output strain values plotted against applied force. These figures show (a) ε_x vs *Fx*, (b) ε_y vs *Fy*, and (c) ε_z vs *Fz*. The vertical axes represent the output strain values and the horizontal axes are the applied forces. The dotted line is an approximation curve obtained by the least squares method to fit the output strain values and to pass through the origin (0, 0). The linear correlation coefficients are shown in each direction.

4. Discussion

In this study, we designed the three-axis force-sensor-instrumented prosthesis. The strain of the sensing element when forces are applied to the force sensor was analyzed by FEM, and it was confirmed that the three components of force can be detected. The calibration results showed that the relationship between the output strain and the applied force was generally consistent with the results of FEM analysis. Therefore, the three-axis force-sensor-instrumented prosthesis developed in this study can measure external forces along three axes.

However, the magnitude of output strain was smaller than the FEM analysis results for all axes, and there were errors in the output strain values. The silicone gasket sandwiched between the upper and bottom parts affects the magnitude of output strain. The silicone gasket supports the upper part, reducing the force applied to the sensing element. In this study, the silicone gasket with a type A durometer hardness of 48 was used because it was readily available and heat- and chemical-resistant, but it would be better to use a softer gasket to increase the output strain. As the output strain increases and the signal-to-noise ratio improves, the measurement variability decreases. In the case of a harder gasket, the force sensor would be more rigid, and the load capacity is larger, but the resolution decreases. It is not known whether the hardness used in this study is the best.

Considering the error, we speculate that the main factor contributing to error is the low strain sensitivity of the force sensor. Owing to the small changes in output strain, the relative effects of unexpected noises, such as thermal strain, PCB noise, and manufacturing tolerances become more pronounced. However, assuming that the material temperatures at all six strain gauge locations were the same, the effects of thermal strain are expected to be cancelled out for the *Fx* and *Fy* directions, as they are calculated from the differential signals of two or more strain gauges. Therefore, we consider that the errors in *Fx* and *Fy* mainly originate from PCB noise and manufacturing tolerances. In particular, the sensing element is fixed to the upper and bottom parts with screws, and it is predicted that the initial strain will also change depending on the tightening torque of these screws. It was so difficult to manufacture the sensing element as a single unit with the upper or bottom parts. Thus, screw fixations are necessary to attach the strain gauges and install the PCB. To mitigate these effects, it is considered effective not only to control the screw tightening torque but also to use screw adhesive during assembly to lock the tightening torque in place. This approach is expected to reduce variations in initial strain caused by mechanical assembly and improve the stability and reproducibility of the strain measurements. For the *Fz* direction, the thermal strains from six strain gauges are added, resulting in a larger error. For example, if the temperature of the sensing element changes by 1 °C, a thermal strain of 17.3 $\mu\varepsilon$ per strain gauge is generated on the basis of the coefficient of thermal expansion of SUS303 (17.3×10^{-6} /°C), resulting in a total of 103.8 $\mu\varepsilon$ for six strain gauges. Given that the coefficient *Cz* is 0.087, the change in *Fz* due to thermal strain is calculated to be approximately 9 N. Therefore, with the current strain sensitivity, the effect of temperature cannot be neglected. However, it is considered that this effect can be mitigated by enhancing the strain sensitivity, for example, by reducing the thickness of the sensing element or by employing a softer gasket.

The force sensor and its performance are compared with those used in a previous study.[16] The force sensor employed in the previous measurements was a capacitive pressure force sensor, which enabled wireless data acquisition. However, the measurements were limited to uniaxial compressive force, with a calibration range from 22 to 311 N; forces below 22 N were not measurable, and within the calibrated range of 22 to 311 N, the maximum error was 31.4 N. In contrast, the force sensor developed in this study can measure forces along three axes. Although its calibration range was up to 30 N, it achieves a maximum error of 13 N at the most.

This study has three limitations. The first is that the force sensor had a maximum error of 13 N. This is mainly due to the gasket reducing the output strain, making the noise larger than the signal. The second limitation is that the output strain could not be temperature- compensated. Owing to a lack of space for wiring, it was not possible to use temperature- compensated strain gauges. Since the patient's body temperature is kept almost constant during surgery,[19] temperature compensation is not considered necessary, but when the signal-to-noise ratio is small, the effect of temperature becomes large. The third limitation is that the calibration force range was limited to up to 30 N. In previous experiments, the shoulder joint contact force was approximately 100 to 200 N.[9,15–17] This report is based on the experiment conducted in the United States; however, the force sensor will be used in Japan, and a small load is expected. Therefore, we placed emphasis on being able to measure a small load accurately.

For future clinical use, there are other required tasks. When used in surgery, the force sensor should be sterilized, but wired connections are cumbersome, so it would be better to make the force sensors wireless. In addition, because the force sensor is only used temporarily during RTSA, a disposable device would be ideal. However, individual calibration is required for each force sensor, and because the force sensors are made of metal, which entails high machining costs and stringent precision requirements, mass production is challenging.

5. Conclusions

In this study, we developed the three-axis force sensor to measure the shoulder joint contact force during RTSA. The sensing element with three measuring elements was designed, and the output strain values obtained when forces were applied to the sensing element were analyzed by FEM. In addition, the relationship between the output strain and the applied force was assumed and verified by calibration. As a result of the calibration, the correlation coefficients between the output strain and the applied force were 0.8284 on the *X*-axis, 0.8078 on the *Y*-axis, and 0.9413 on the *Z*-axis. The maximum errors were 8.5 N on the *X*-axis, −13 N on the *Y*-axis, and −6.1 N on the *Z*-axis.

Author Contributions

Yusuke Hirai designed and analyzed the force sensor and wrote the paper. Yuta Onishi manufactured the force sensor. Masaru Higa supervised this study and reviewed the paper.

Conflicts of Interests

The authors declare no conflicts of interest.

References

1 P. Boileau, D. Watkinson, A. M. Hatzidakis, and I. Hovorka: J. Shoulder Elbow Surg. **15** (2006) 146. https://doi.org/10.1016/j.jse.2006.01.003
2 T. Bufquin, A. Hersan, L. Hubert, and P. Massin: Bone Joint J. **89** (2007) 516. https://doi.org/10.1302/0301-620X.89B4.18435
3 M. Walker, M. P. Willis, J. P. Brooks, D. Pupello, P. Mulieri, and M. A. Frankle: J. Shoulder Elbow Surg. **21** (2012) 514. https://doi.org/10.1016/j.jse.2011.03.006
4 C. Levigne, M. Chelli, T. R. Johnston, M. C. Trojani, D. Mole, G, Walch, and P. Boileau: J. shoulder Elbow Surg. **30** (2021) 2312. https://doi.org/10.1016/j.jse.2021.01.033
5 N. B. Jain and K. Yamaguchi: J. Shoulder Elbow Surg. **23** (2014) 1905. https://doi.org/10.1016/j.jse.2014.06.055
6 S. A. Parada, P. H. Flurin, T. W. Wright, J. D. Zuckerman, J. A. Elwell, C. P. Roche, and R. J. Friedman: J. Shoulder Elbow Surg. **30** (2021) 811. https://doi.org/10.1016/j.jse.2020.07.028
7 M. A. Zumstein, M. Pinedo, J. Old, and P. Boileau: J. Shoulder Elbow Surg. **20** (2011) 146. https://doi.org/10.1016/j.jse.2010.08.001
8 R. A. Gallo, S. C. Gamradt, C. J. Mattern, F. A. Cordasco, E. V. Craig, D. M. Dines, R. F. Warren, and Sports Medicine and Shoulder Service at the Hospital for Special Surgery NY: J. Shoulder Elbow Surg. **20** (2011) 584. https://doi.org/10.1016/j.jse.2010.08.028
9 M. Walker, J. Brooks, M. Willis, and M. Frankle: Clin. Orthop. Relat. Res. **469** (2011) 2440. https://doi.org/10.1007/s11999-011-1892-0
10 K. W. Farmer, M. Higa, S. Banks, C. C. Chang, A. M. Struk, and T. W. Wright: J. Exp. Orthop. **7** (2020) 98. https://doi.org/10.1186/s40634-020-00311-0
11 G. Bergmann, F. Graichen, A. Bender, M. Kaab, A. Rohlmann, and P. Westerhoff: J. Biomech. **40** (2007) 2139. https://doi.org/10.1016/j.jbiomech.2006.10.037
12 P. Westerhoff, F. Graichen, A. Bender, A. Halder, A. Beier, A. Rohlmann, and G. Bergmann: J. Biomech. **42** (2009) 1840. https://doi.org/10.1016/j.jbiomech.2009.05.035
13 G. Bergmann, F. Graichen, A. Bender, A. Rohlmann, A. Halder, A. Beier, and P. Westerhoff: J. Biomech. **44** (2011) 1543. https://doi.org/10.1016/j.jbiomech.2011.02.142
14 M. Verstraete, M. Conditt, M. Parsons, J. Decerce, G. Goodchild, A. Greene, and C. Roche: EPiC Series in Health Sciences **3** (2019) 398. https://doi.org/10.29007/dlq8
15 M. Higa, C. C. Chang, C. Roche, A. M. Struk, K. W. Farmer, T. W. Wright, and S. A. Banks: Sens. Mater. **30** (2018) 1989. https://doi.org/10.18494/SAM.2018.1940
16 M. A. Verstraete, M. A. Conditt, I. M. Parsons, A. T. Greene, C. P. Roche, J. Decerce, R. B. Jones, A. R. Youderian, T. W. Wright, and J. D. Zuckerman: JSESArthro. **30** (2020) 2. https://doi.org/10.1053/j.sart.2020.03.001
17 F. Graichen, R. Arnold, A. Rohlmann, and G. Bergmann: IEEE Trans. Biomed. Eng. **54** (2007) 253. https://doi.org/10.1109/TBME.2006.886857
18 K. Hoffmann: Applying the Wheatstone Bridge Circuit (HBM, Darmstadt, 1974) 7.
19 B. Bindu, A. Bindra, and G. Rath: J. Anaesthesiol. Clin. Pharmacol. **33** (2017) 306. https://doi.org/10.4103/joacp.JOACP_334_16